ACS APPLIED MATERIALS & INTERFACES

Research Article

www.acsami.org

2D Cross Sectional Analysis and Associated Electrochemistry of Composite Electrodes Containing Dispersed Agglomerates of Nanocrystalline Magnetite, Fe_3O_4

David C. Bock,[†] Kevin C. Kirshenbaum,[‡] Jiajun Wang,[‡] Wei Zhang,[‡] Feng Wang,[‡] Jun Wang,[‡] Amy. C. Marschilok,*[,†,§] Kenneth J. Takeuchi,*[,†,§] and Esther S. Takeuchi*[,†,‡,§]

[†]Department of Chemistry, Stony Brook University, Stony Brook, New York 11794, United States

[‡]Brookhaven National Laboratory, Upton, New York 11973, United States

[§]Department of Materials Science and Engineering, Stony Brook University, Stony Brook, New York 11794, United States

Supporting Information

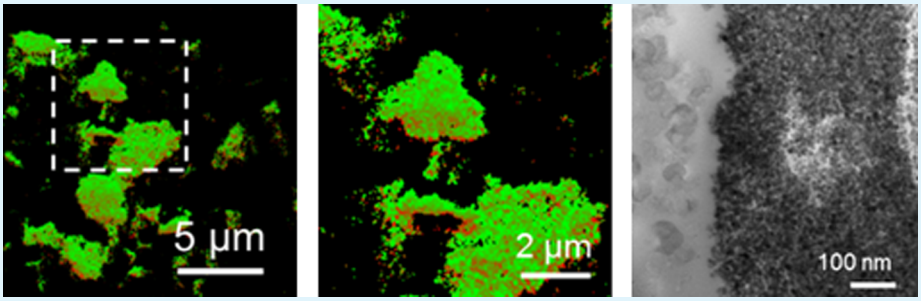

ABSTRACT: When electroactive nanomaterials are fully incorporated into an electrode structure, characterization of the crystallite sizes, agglomerate sizes, and dispersion of the electroactive materials can lend insight into the complex electrochemistry associated with composite electrodes. In this study, composite magnetite electrodes were sectioned using ultramicrotome techniques, which facilitated the direct observation of crystallites and agglomerates of magnetite (Fe_3O_4) as well as their dispersal patterns in large representative sections of electrode, via 2D cross sectional analysis by Transmission Electron Microscopy (TEM). Further, the electrochemistry of these electrodes were recorded, and Transmission X-ray Microscopy (TXM) was used to determine the distribution of oxidation states of the reduced magnetite. Unexpectedly, while two crystallite sizes of magnetite were employed in the production of the composite electrodes, the magnetite agglomerate sizes and degrees of dispersion in the two composite electrodes were similar to each other. This observation illustrates the necessity for careful characterization of composite electrodes, in order to understand the effects of crystallite size, agglomerate size, and level of dispersion on electrochemistry.

KEYWORDS: *magnetite, crystallite size, agglomerate, transmission X-ray microscopy, lithium-ion battery, ultramicrotome*

INTRODUCTION

New scientific paradigms in battery science and technology are needed to address energy issues associated with grid storage, electric vehicles, and portable electronics, where both energy content and power are critical aspects of performance.[1,2] Specifically, a critical ongoing battery challenge is the narrowing of the often considerable gap between theoretical energy content and realizable energy delivery of energy storage systems. While battery voltage and energy content can be estimated theoretically from electrode chemical compositions, the functional delivered energy from a battery also depends to a substantial extent on the physical properties of the electrode materials, where the dimensions of active material particles as well as the electrode design can have a large effect on the discharge characteristics and cycling performance of batteries.[3−6] Detailed understanding of the roles of various material properties and their systems level interactions within a battery should ultimately lead to future energy storage devices which can address critical applications which already exist.

The favorable impact of nanosized materials has been reported for several active materials including $LiCoO_2$, $LiFePO_4$, $LiNi_{0.5}Mn_{1.5}O_4$, and $Ag_xMn_8O_{16}$, where reducing the crystallite dimension of active materials shortens the total path length for Li ion diffusion yielding increased delivered capacity at high discharge currents by increasing the utilization of the active material.[7−16] Such considerations are especially important for densely structured electroactive materials such as magnetite (Fe_3O_4), which has an inverse spinel structure. Accordingly, several studies report the impact of crystallite size on nanocrystalline Fe_3O_4 electrochemistry.[17−23] Specifically,

Received: March 21, 2015
Accepted: May 29, 2015
Published: May 29, 2015

DOI: 10.1021/acsami.5b02478
ACS Appl. Mater. Interfaces 2015, 7, 13457−13466

the improvement in the electrochemical performance with decreasing crystallite size was seen with an increase in loaded voltage, thus decreased polarization. Results of an XAS study suggest that the surface of Fe_3O_4 crystallites is rich in Fe^{3+} because of surface oxidation.[22] For smaller sized crystallites with high surface area, enhancement of electrochemical capacity may be in part due to this net enrichment of Fe_3O_4 in Fe^{3+}.[22] However, surface oxidation does not fully account for improvements in electrochemical performance, and as such kinetic effects of crystal size on the transport of Li ions are expected to play a key role.

Battery electrodes are composites by necessity, as the electroactive material must be mixed with conductive additive to form a percolation network and sufficient binder to achieve mechanical integrity.[24] Thus, in addition to crystallite size of the electroactive material, agglomeration, and agglomerate distribution may also affect battery electrochemistry and thus warrant further study. However, there are few literature reports which quantify agglomeration and agglomerate distribution within battery electrodes. Two reports suggest that the level of material agglomeration in battery electrodes, due to changes in processing, can affect battery electrochemistry, but no measurement of the agglomerates was provided.[25,26] Similarly, in the prior studies which investigated the impact of crystallite size on Fe_3O_4 electrochemistry, agglomeration of magnetite contained within the subject electrodes was not directly characterized.[17−23]

A complete study of an electroactive nanomaterial in the complex environment of a composite battery electrode should consider agglomerate size as well as inherent crystallite size of the nanomaterial as both factors can influence electronic conductivity as well as access to lithium ions. This work stands in contrast to previous studies which have considered only the effects of crystallite size on electrochemical performance. This study presents methodology whereby large areas of the electrode can be probed to assess the agglomerate sizes and distribution of nanomaterials when incorporated into a composite electrode.

Focused ion beam (FIB) techniques have previously been reported for obtaining cross sections of battery electrodes for further examination.[27−35] Cross-sectional samples are excised using an FIB milling technique, whereby trenches are ion-milled normal to the electrode surface to produce a thin lamella. The lamella is then cut free and lifted out from the bulk sample using a tungsten manipulator welded to the free part of the sample.[27,28] Notably, the samples are cut normal to the plane of the electrode and typically have dimensions of 20−40 μm. Information at a local agglomerate level can be gained, but may not be fully representative of the larger electrode surface. In contrast to FIB, use of an ultramicrotome enables preparation of characterizable electrode samples at millimeter scale. Only one previous report has described this technique for investigation of battery electrodes.[36]

In this study, composite electrodes containing magnetite, Fe_3O_4, powders of two different crystallite sizes were prepared, characterized, and electrochemically evaluated. An ultramicrotome diamond knife was utilized to cut electrode sections with large area (1 × 2 mm), where the cut sections were parallel, rather than perpendicular, to the electrode surface. This technique enabled large areas of uniform thickness to be viewed by TEM for broader determination of electrode morphology. In addition to the TEM examination of sectioned electrodes, 2D mapping via transmission X-ray microscopy (TXM) combined with X-ray absorption near edge spectroscopy (XANES) was used to construct a 2D map of the electrode where the distribution of the iron and the iron oxidation states were determined prior to and after partial reduction.

Thus, we are able to quantify agglomerate size of the active material within functional electrodes which yielded the unexpected outcome that the agglomerate sizes of the magnetite samples were not dependent on crystallite size, as would have been expected based on prior particle size measurements.[19,20] The electrochemical results indicated less polarization and higher delivered energy during discharge/charge cycling for the smaller crystallite size material with comparable agglomerate size and distribution. This provided new insights into the agglomerate sizes and discharge progress of nanocrystalline materials when incorporated into electrodes. We expect this approach to be useful in characterizing other electrode materials where agglomeration of small particles in an electrode may influence electrochemical performance.

EXPERIMENTAL SECTION

Magnetite, Fe_3O_4, was synthesized using a previously reported coprecipitation approach, utilizing aqueous solutions of iron(III) chloride hexahydrate, iron(II) chloride hexahydrate, and triethylamine.[19,20] Larger sized nanocrystalline magnetite, ∼30 nm, was purchased from Alfa Aesar.

X-ray diffraction data was collected using a Rigaku Smart Lab diffractometer with Cu Kα radiation. Collected data were analyzed using MDI Jade software. The crystallite sizes of the Fe_3O_4 powders were calculated by applying the Scherrer equation to the fwhm of the (311) peak. An instrumental broadening correction was applied using a LaB_6 standard. Multipoint BET (Brunauer, Emmett, Teller) surface area data were collected using $N_2(g)$ as adsorbant using a Quantachrome Nova 4200e instrument.

Electrode coatings were prepared on aluminum foil substrates with the ratio 42.5% Fe_3O_4, 42.5% acetylene black carbon, and 15% polyvinylidene fluoride binder (PVDF). A slurry was prepared by mixing carbon, Fe_3O_4 and *N*-methyl-2-pyrrolidone (NMP) in a planetary centrifugal mixer. PVDF dissolved in NMP was then added and additional mixing was performed until the slurry was homogeneous. The slurry was cast onto an aluminum (Al) foil and dried under vacuum to remove solvent. Electrochemical tests were performed using coin-type experimental cells with lithium metal anodes and 1 M $LiPF_6$ in 1:1 dimethyl carbonate: ethylene carbonate electrolyte. In this study Fe_3O_4 was tested as a half cell versus lithium metal to accurately measure the voltage of the iron oxide at selected discharge levels. Testing was conducted for the cells incorporating 28 or 8 nm Fe_3O_4 to 800 mAh/g using a 2.4 $\mu A/cm^2$ current density to determine differences in polarization as a function of discharge. Lithium/magnetite, Li/Fe_3O_4, cell cycling data was collected by discharging three groups of cells to 100 mAh/g with a secondary limit of 1.0 V and current densities of 2.4, 4.8, or 24 $\mu A/cm^2$ followed by charge to 3.0 V under the same rate as the discharge. Additional cells used for the TXM experiments were discharged to 100 mAh/g at 24 $\mu A/cm^2$ current density with no charging step. Post discharge, electrodes were recovered in an inert atmosphere glovebox and were sealed in polyimide tape to prevent oxidation during the TXM experiments.

TEM images of the nondischarged electrodes were obtained by embedding the samples in resin. During the embedding process, the samples were placed under vacuum to improve permeation of the resin. Ultrathin electrode sections of 80 nm were cut with a Reichert-Jung UltracutE ultramicrotome and placed on Formvar coated mesh copper grids. Sections were viewed with a FEI Tecnai12 BioTwinG^2 transmission electron microscope. Digital images were acquired with an AMT XR-60 CCD Digital Camera system.

DOI: 10.1021/acsami.5b02478
ACS Appl. Mater. Interfaces 2015, 7, 13457−13466

Samples for TXM were prepared by disassembling coin cells under inert atmosphere, recovering the cathodes and placing them between polyimide tape. Pristine and discharged Fe_3O_4 coatings were analyzed using transmission X-ray microscopy (TXM) in combination with X-ray absorption near edge structure (XANES) spectroscopy at Beamline X8C, NSLS I, Brookhaven National Laboratory where 40 μm × 40 μm areas of the electrode coatings were mapped. X-ray Absorption Near Edge Structure (XANES) image series were collected by scanning the Fe absorption K-edge from 7092 to 7192 eV, with 2 eV step size, and one image per step. Image series were collected with 20 s exposure time, and 2 × 2 pixels binned camera pixels, where each binned pixel is approximately 39 × 39 nm^2. Additional 2 × 2 binning was used during data processing resulting in 78 nm × 78 nm resolution. The distributions of standard phases Fe_3O_4 and FeO were analyzed by least-squares combination fitting using a customized MatLab program developed at Beamline X8C.

The public domain Java image processing program ImageJ[37] was used to analyze the size and agglomerate distributions from the TEM and TXM images. Images were converted to greyscale, and a threshold was applied. After spatial calibration using the scale bar from the TEM or TXM image, a sizing algorithm was applied, resulting in tabular data and a corresponding indexed image. The indexed images and table were visually inspected to ensure that all size distributions were accurate.

RESULTS AND DISCUSSION

Material Synthesis and Characterization. Synthesized nanocrystalline Fe_3O_4 samples were prepared as previously reported using a coprecipitation approach,[19,20] while the larger crystallite size Fe_3O_4 was purchased. The Fe_3O_4 samples were characterized by X-ray diffraction and the patterns compared well with the reported reference pattern[21] (PDF 01-088-0315) with no additional peaks observed. The crystallite sizes of the Fe_3O_4 powders were calculated from the XRD data by applying the Scherrer equation[38,39] to the fwhm of the (311) peak including correction for instrumental broadening using a LaB_6 standard. Crystallite sizes determined by this method were 28 and 8.7 nm for the purchased and synthesized Fe_3O_4 materials, respectively. Transmission electron microscopy (TEM) imaging confirmed the size difference between the two material samples, Figure 1. The TEM data were analyzed using ImageJ

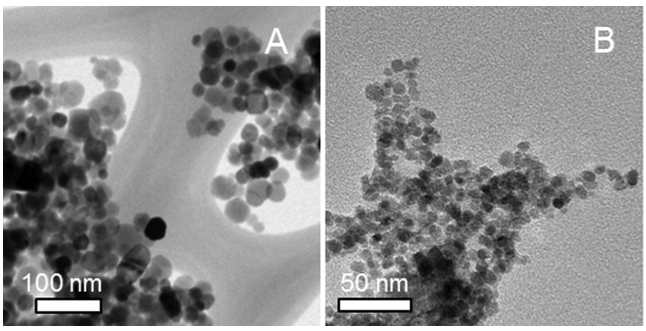

Figure 1. TEM of (A) 28 nm Fe_3O_4 sample and (B) 8 nm Fe_3O_4 sample.

software[37] and indicated average sizes of 32 ± 11 and 7.3 ± 1.4 nm for the two samples showing reasonable correspondence to the values determined by XRD.

Surface area of the Fe_3O_4 materials was investigated using the multipoint BET method. The surface area by BET of the materials was determined for the small and large crystallite size materials to be 140 ± 7 and 32 ± 4 m^2/g, respectively. From these measurements, average particle diameter was calculated to be 8.5 and 36 nm for synthesized and commercial materials, respectively, using a density of 5.17 g/cm^3 for Fe_3O_4 and assuming that the particles were spherical and nonporous. The calculated particle diameter values compare well with values obtained from XRD and TEM.

Electrode Characterization. The Fe_3O_4 samples were utilized to prepare electrodes as described in the Experimental Section. The environment of the active Fe_3O_4 materials within the nondischarged electrodes was investigated where the electrodes were sectioned parallel to the plane of the electrode and imaged using TEM. Figure 2 shows bright-field TEM

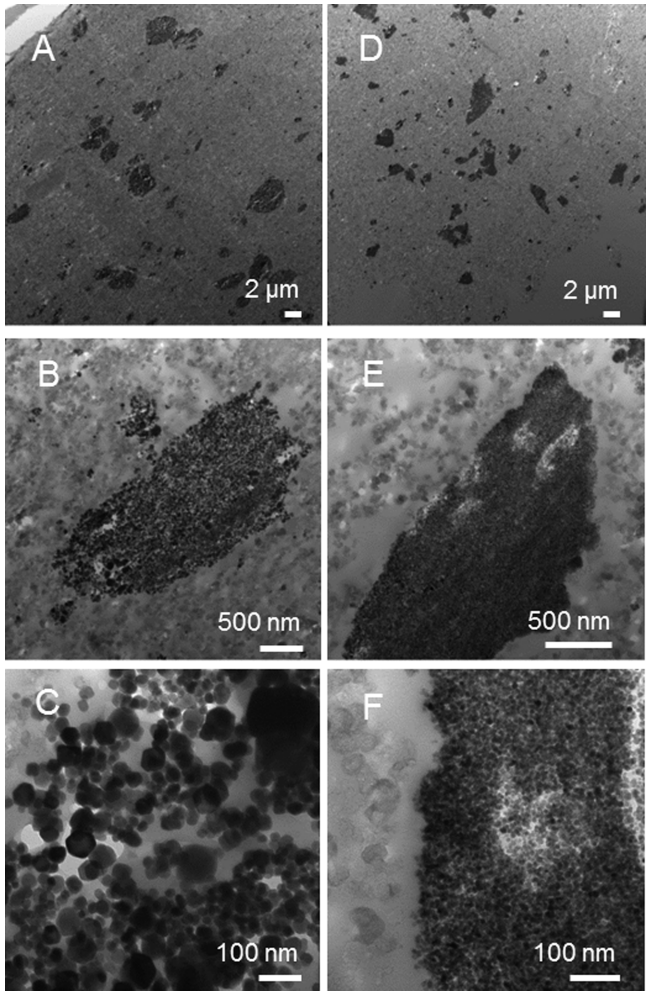

Figure 2. Bright-field TEM images of sectioned electrodes fabricated with the 28 nm sized Fe_3O_4 (images A–C) and 8 nm sized Fe_3O_4 (images D–F).

images of sectioned electrodes fabricated with the 28 nm sized Fe_3O_4 (images A, B, and C) and 8 nm sized Fe_3O_4 (images D, E, and F). In both types of Fe_3O_4 electrodes, large, irregularly shaped agglomerates (in dark contrast) of Fe_3O_4 crystallites are apparent. While the crystallite sizes of the two magnetite samples Fe_3O_4 are different by a factor of 3, the observed sizes of the agglomerates within the electrodes were of the same order of magnitude, with the majority of the active material contained in large agglomerates of diameters of 0.5–6 μm.

The TEM images are representative of the known ratio of active/inactive materials in the composite. Using a bulk density of 0.88 g/cm^3 for the Fe_3O_4 nanopowder, a bulk density of 0.1

DOI: 10.1021/acsami.5b02478
ACS Appl. Mater. Interfaces 2015, 7, 13457–13466

g/cm^3 for carbon, and density of 1.78 g/cm^3 for the PVDF binder, the percent volume of Fe_3O_4 in the composite is calculated to be 10%. From the TEM cross sectional images, the average percent area of Fe_3O_4 is 12%, showing good agreement with the calculated value.

Direct determination of the size of the aggregates was done by analysis of the sectioned electrode TEM images using ImageJ software.[37] Aggregate areas were measured and the average diameter of those areas was calculated. Average diameters of the aggregates were 1.3 ± 1.2 (n = 261) and 1.3 ± 1.1 μm (n = 244) for the 28 and 8 nm crystallite size samples, indicating a similar level of aggregation for the two samples. The distribution of aggregate diameters is shown in Figure 3.

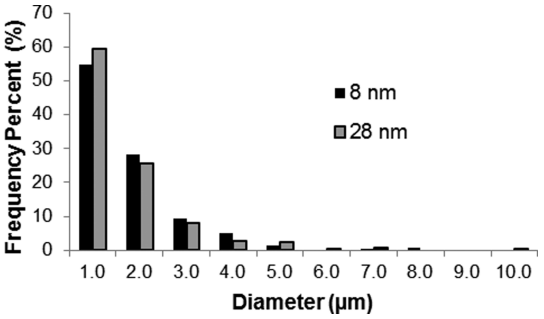

Figure 3. Aggregate size distributions in electrodes prepared with 28 and 8 nm Fe_3O_4.

For both samples, the frequency of the aggregates decreased with increasing size, with over 60% of the aggregates having an average diameter below 1.0 μm. Approximately 30% of the aggregates had an average diameter between 1.0−4.0 μm, while less than 5% had diameter greater than 5.0 μm.

The size of the Fe_3O_4 crystallites was also measured from TEM images of the sectioned electrodes. Average Fe_3O_4 crystallite sizes were determined to be 32 ± 9 nm and 9.3 ± 1.4 and 32 ± 9 nm for the synthesized and commercial materials, respectively. These values compare well with the particle sizes determined from Scherrer analysis of the XRD data and indicate that the electrode processing steps did not change the size of the Fe_3O_4 crystallites.

The first nearest-neighbor distance method was used to quantify the spatial dispersion between aggregates of Fe_3O_4 in the sectioned electrode TEM images. Nearest neighbor methods are widely used to quantify dispersion in composites.[40−45] In this technique, the nearest neighbor distance r is defined as the distance between the centroid of a particle and that of its nearest neighbor.[44] For n number of particles, with specified particle density ρ, the mean nearest neighbor distance is $\overline{r}_A = (\Sigma r/n)$.[46] Density ρ is defined as $\rho = (n/s)$, where there are n particles in study area S.[47] If the particles are distributed at random, the mean nearest neighbor distance is $\overline{r}_E = (1/(2\sqrt{\rho}))$. Thus, the ratio $R = (\overline{r}_A/\overline{r}_E)$ may be used as an index to determine whether the observed distribution of particles in a sample varies from the expected random distribution.[46] For maximum aggregation, R = 0, while R = 1 indicates a random arrangement, and R = 2.149 for a prefect dispersion.[46]

A distribution of the nearest neighbor distances for aggregates in the sectioned electrodes prepared with 28 and 8 nm Fe_3O_4 is shown in Figure 4. The calculated values of R were 1.10 (n = 261) and 1.16 (n = 244) and for 28 and 8 nm Fe_3O_4, respectively. These index values indicate that the Fe_3O_4 aggregates are randomly dispersed in the electrode coatings,

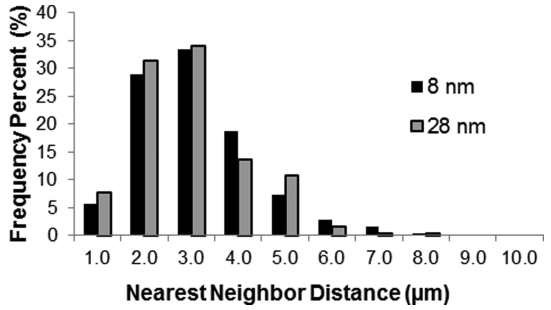

Figure 4. Nearest neighbor distance distributions of aggregates in electrodes prepared with 28 and 8 nm Fe_3O_4.

and that a similar level of dispersion among aggregates is observed irrespective of Fe_3O_4 crystallite size. The same ratio of active material, carbon, and binder additives were used for both particle sizes in order to reliably compare the electrochemistry of the two samples. The consistent experimental preparation is believed to contribute to the similarity of aggregation observed experimentally. Magnetite nanoparticles have superparamagnetic character due to their finite size and thus exhibit limited magnetic interaction at room temperature in the absence of a magnetic field compared with bulk magnetite.[48,49] Consequently, magnetic moments of nanosized Fe_3O_4 particles were expected to insignificantly contribute to the observed agglomeration.

Electrochemical Evaluation. Coin type cells were assembled with lithium anodes and 1 M $LiPF_6$ ethylene carbonate: dimethyl carbonate electrolyte. Cells utilizing cathodes with the 28 or 8 nm Fe_3O_4 were discharged to 800 mAh/g, Figure 5. Large differences in the loaded cell voltage

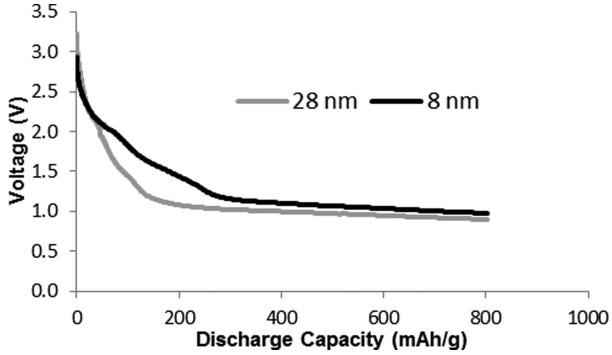

Figure 5. Representative discharge curves for 28 nm crystallite size and 8 nm crystallite size Fe_3O_4 material discharged to 800 mAh/g, with a 1 V cutoff, using a 2.4 μA/cm^2 current density.

were observed between 50 and 250 mAh/g, while at higher depths of discharge the voltage profiles for the two cell types were similar. Differences in polarization as a function of discharge likely result from the different lithiation mechanisms which occur during the reduction of Fe_3O_4. The structures of nonlithiated, pristine Fe_3O_4[50] and the lithiated phase $Li_2Fe_3O_4$[51] are shown in Figure 6. Magnetite crystallizes in an inverse spinel structure, with Fe^{3+} occupying tetrahedral holes (Wyckoff position 8a) and both Fe^{3+} and Fe^{2+} occupying octahedral holes (Wyckoff position 16d) in a cubic close packed array of O^{2-} ions, Figure 6A.[50] During the initial lithiation (x < 2) process, Li^+ ions insert into vacant octahedral (16c) sites.[51,52] At low Li^+ concentration, electrostatic repulsion

DOI: 10.1021/acsami.5b02478
ACS Appl. Mater. Interfaces 2015, 7, 13457−13466

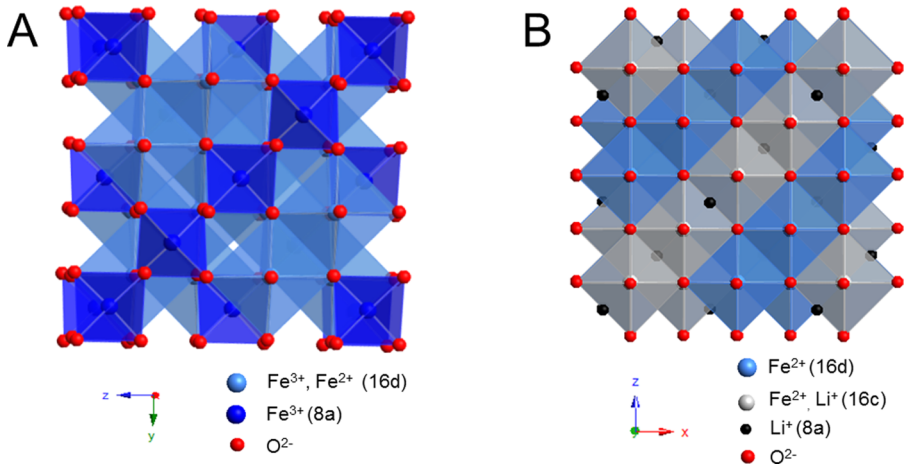

Figure 6. Crystal structure of (A) magnetite, Fe_3O_4, and (B) lithiated magnetite, $Li_2Fe_3O_4$. In the inverse spinel structure of Fe_3O_4, Fe^{3+} occupies tetrahedral holes (Wyckoff position 8a) and both Fe^{3+} and Fe^{2+} occupy octahedral holes (Wyckoff position 16d) in a cubic close packed array of O^{2-} ions. $Li_2Fe_3O_4$ is a rocksalt-like phase, with tetrahedral Fe ions shifted to adjacent octahedral holes (Wyckoff position 16c). Li^+ ions fill additional octahedral holes and tetrahedral holes.

displaces 8a Fe ions into the 16c site. Additional Li ions fill octahedral holes (16c) and the now empty tetrahedral holes, and the result of this initial insertion mechanism is the transformation of the $A[B_2]O_4$ spinel phase to a $(LiA)[B_2]O_4$ rocksalt type phase, Figure 6B.[51,52] Initial lithiation via the insertion mechanism yields a theoretical capacity of 230 mAh/g. Further lithiation is proposed to form Li_2O and α-Fe metal,[52] supported by recent X-ray absorption spectroscopy results.[23] Conversion of $Li_2Fe_3O_4$ to Li_2O and α-Fe metal yields an additional 690 mAh/g of capacity. At the 100 mAh/g (0.86 electron equivalent) discharge level, used in subsequent cycling experiments, lithiation/delithiation occurs via the insertion/deinsertion mechanism. The cubic close packed array of oxygen atoms remains intact, and the differences in polarization between large/small crystallite samples would then be attributable to differences in Li^+ diffusion length. In contrast, at higher discharge levels where the conversion reaction is the dominant lithiation mechanism, the difference in polarization due to crystallite size is smaller and may result from the dramatic structural changes during the advanced discharge process.

Further electrochemical testing was performed at the 100 mAh/g reduction level with a discharge limit of 1.0 V versus Li to focus on the insertion mechanism that occurs upon initial lithiation, and the associated differences in polarization for large and small crystallite size samples. Three groups of cells were discharged to 100 mAh/g with a voltage limit of 1.0 V using current densities of 2.4, 4.8, or 24 $\mu A/cm^2$ followed by charge to 3.0 V under the same rate as the discharge. Cells utilizing the smaller 8 nm crystallite size Fe_3O_4 material exhibited significantly reduced polarization, resulting in higher cell loaded voltage, Figure 7A, where the data discharge using the 2.4 or 24 $\mu A/cm^2$ current densities are shown. Note that under the 24 $\mu A/cm^2$ current density, the 28 nm Fe_3O_4 sample cells showed significant polarization, and reached the 1.0 V limit prior to delivering the full 100 mAh/g. Polarization, or overpotential, describes the deviation of the observed loaded voltage from the thermodynamic open circuit potential.[53] Under the 2.4 $\mu A/cm^2$ current density, the smaller crystallite size samples consistently delivered specific energy ~18% higher than the larger crystallite size samples through 30 cycles, Figure 7B. Specific energy (Ah/g × voltage) is used to present the data in order to highlight the impact of the differences in polarization for the samples as a function of crystallite size. Under the 4.8 $\mu A/cm^2$ current density, the 28 nm Fe_3O_4 containing cells delivered 160 mWh/g on cycle 10 compared to 180 mWh/g by the 8 nm Fe_3O_4 cells. However, under the 24 $\mu A/cm^2$ current density, the 28 nm Fe_3O_4 containing cells delivered 74 mWh/g on cycle 10 compared to 170 mWh/g by the 8 nm Fe_3O_4 cells, where the smaller crystallite sized magnetite again delivered higher energy in this case by >200%, Figure 7C. After 30 cycles at 24 $\mu A/cm^2$ current density, the smaller crystallite sized magnetite showed >170% higher energy delivery than the large crystallite sized material. The correlation between smaller Fe_3O_4 crystallite size and improved electrochemical performance is consistent with previous studies and was attributed to higher surface area and shorter Li^+ ion diffusion distance.[19,20,22,23] Notably, even though similar levels of Fe_3O_4 agglomeration and levels of dispersion were seen in electrodes prepared from 28 and 8 nm samples of Fe_3O_4, significantly different electrochemistry was observed, providing evidence that the size of the Fe_3O_4 crystallites is a critical factor affecting electrochemical performance.

The crystal sizes of Fe_3O_4 particles in the composite electrodes were calculated before and after cycling using by applying the Scherrer equation to collected X-ray diffraction patterns. Before cycling, Fe_3O_4 crystal sizes were determined to be 31 and 9 nm for electrodes prepared using purchased and synthesized Fe_3O_4 materials, respectively. After 30 cycles, the electrodes were recovered from the cells and XRD patterns were again measured. Post cycling, Fe_3O_4 crystal sizes were unchanged at 30 and 9 nm. This result shows that at the cycling level used, the Fe_3O_4 active materials were able to lithiate/delithiate effectively without degradation to an amorphous phase.

Characterization of Electrochemically Reduced Magnetite. Cells were discharged to 100 mAh/g under the 2.4 $\mu A/cm^2$ current density for use in the transmission X-ray microscopy (TXM) experiments to probe differences in discharge between 28 and 8 nm Fe_3O_4 samples. Both undischarged and discharged Fe_3O_4 coatings were analyzed using TXM in combination with X-ray absorption near edge structure (XANES) spectroscopy. Traditional near-edge spectroscopy (XANES) measurements can only be used to

DOI: 10.1021/acsami.5b02478
ACS Appl. Mater. Interfaces 2015, 7, 13457−13466

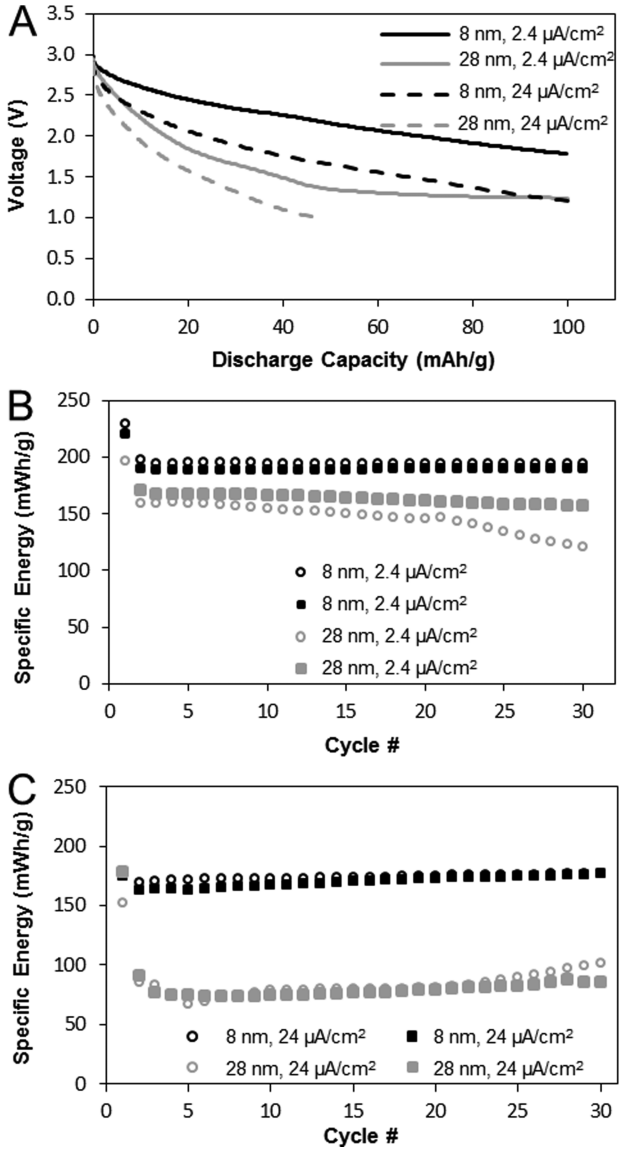

Figure 7. Electrochemical evaluation of composite electrodes. (A) Representative discharge curves for 28 nm crystallite size and 8 nm crystallite size Fe_3O_4 material discharged to 100 mAh/g, with a 1 V cutoff, using a 2.4 $\mu A/cm^2$ (solid trace) or 24 $\mu A/cm^2$ (dashed trace) current density. (B, C) Specific energy versus cycle number for two cells each containing 28 nm (gray) and 8 nm (black) crystallite size Fe_3O_4 material discharged to 100 mAh/g using 2.4 (B) and 24 $\mu A/cm^2$ (C) current density.

determine the average oxidation state of an electrode material where averaging the results of XANES measurements over a large area obscures the possible inhomogeneity resulting from agglomeration or uneven discharge. In contrast, TXM combined with XANES has been used recently to study electrochemical changes of particles and agglomerates in battery materials as it can provide elemental and oxidation-state information pixel by pixel with up to 10 nm (one pixel size) spatial resolution.[54−62] Using an area detector, it is possible to create a 2D profile of the phase distribution within individual particles or agglomerates to observe the reduction of the iron oxidation state as a function of spatial location. This technique enabled mapping of the Fe oxidation state across 40 × 40 μm^2 areas of the electrode coatings to probe the relationships between electrochemical discharge and particle morphology.

TXM-XANES images from the nondischarged, Figure 8, and partially discharged electrode coatings discharged to 100 mAh/g prepared with 28 nm Fe_3O_4 and 8 nm Fe_3O_4, respectively, are shown in Figures 9 and 10. Green and red pixels represent XANES spectra which have been fit to the spectra for reference materials Fe_3O_4 and FeO, respectively (Supporting Information Figure S1). Predominantly green pixels shown by the nondischarged samples confirmed that the oxidation state is consistent with that of Fe_3O_4. The relatively thin electrode and low concentration of active material in the prepared electrodes enabled the resolution of individual Fe_3O_4 agglomerates with minimal overlap. The images indicate that the majority of the active material is concentrated in agglomerates, with the size of the agglomerates corresponding well to the TEM images of the cross-sectioned electrodes. The agglomerate size of the discharged Fe_3O_4 particles is similar to that of the nondischarged samples, suggesting that large changes in morphology do not occur upon reduction to this level.

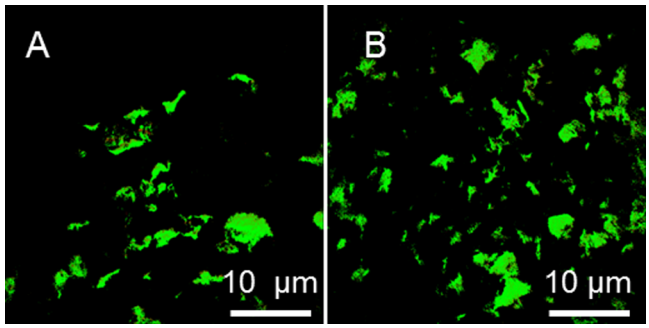

Figure 8. TXM images of (A) nondischarged 28 nm Fe_3O_4 coating and (B) nondischarged 8 nm Fe_3O_4 coating.

Theoretical capacity of composite electrodes is complicated by the capacity contribution of the carbon additive, which will insert lithium at the same voltage as Fe_3O_4. Often times, this contribution is not considered in composite electrodes. However, in this study, the TXM measurement can be used to accurately measure the level of active material reduction in the composite electrode by measuring the oxidation state change of the Fe_3O_4 in the composite upon lithiation. In the TXM images of discharged electrodes, the percentages of reduced (red) areas were 16% and 14% for electrodes utilizing 8 nm Fe_3O_4 and 30 nm Fe_3O_4, respectively. In a 100% Fe_3O_4 electrode without carbon additive we would expect that 43.5% of green (Fe_3O_4) pixels would covert to red (FeO) pixels at 100 mAh/g, the discharge level selected for the electrodes used in the TXM experiments. However, the acetylene carbon black adds additional capacity to the electrode and a lower amount of Fe^{3+} reduction is expected. An 85% acetylene carbon black, 15% PVDF electrode was discharged versus lithium using the same current density as Fe_3O_4/carbon composite electrodes. Based on the measured capacity of the acetylene carbon black in the voltage region of interest and the ratio of Fe_3O_4: carbon in the composite electrodes, approximately 18% of Fe_3O_4 in the composite electrodes should be converted to FeO at the selected discharge level. The analysis of the TXM results shows approximately 15% conversion, which shows reasonable agreement with predicted values. This level of conversion

DOI: 10.1021/acsami.5b02478
ACS Appl. Mater. Interfaces 2015, 7, 13457−13466

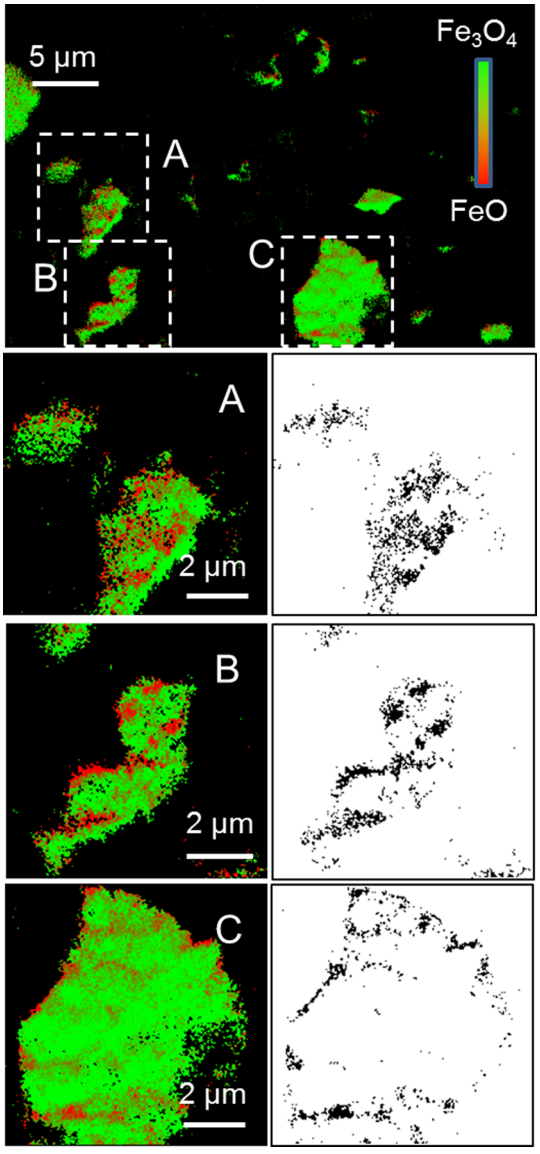

Figure 9. TXM-XANES image of electrode prepared with 28 nm Fe_3O_4 discharged to 100 mAh/g. Selected regions (A–C) are magnified. Black pixels in the corresponding black and white images emphasize the reduced areas of the electrode.

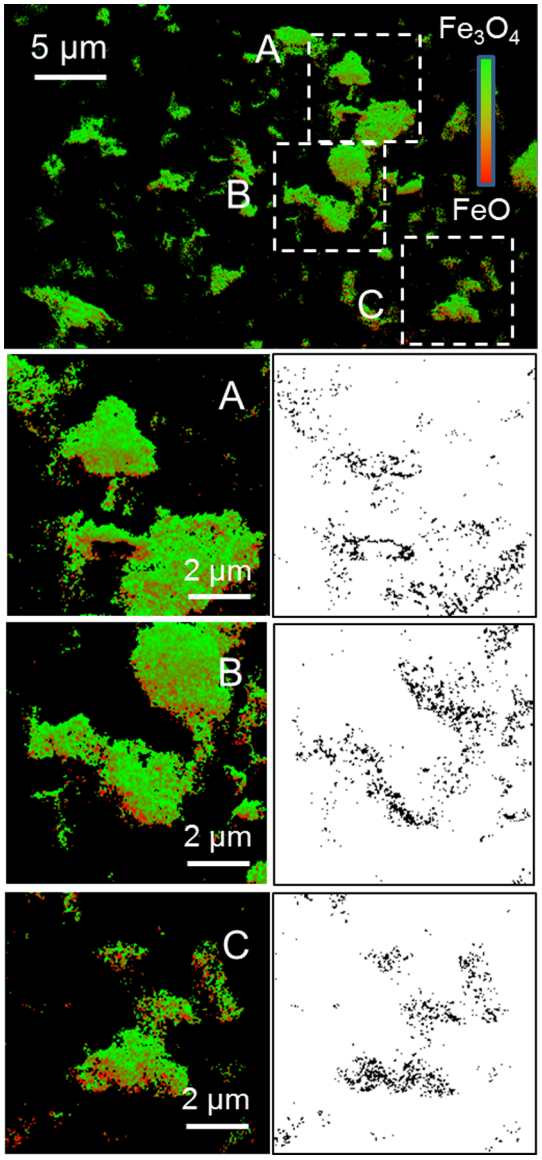

Figure 10. TXM-XANES image of electrode prepared with 8 nm Fe_3O_4 discharged to 100 mAh/g. Selected regions (A–C) are magnified. Black pixels in the corresponding black and white images emphasize the reduced areas of the electrode.

corresponds to approximately 0.3 equiv of lithium insertion into the host spinel structure.

Overall, the appearance of the partially discharged electrode coatings discharged to 100 mAh/g prepared with 28 nm Fe_3O_4 and 8 nm Fe_3O_4 is generally similar where large agglomerates are apparent in each with areas of partially reduced Fe_3O_4. However, a closer examination suggests a more uniform distribution of reduced material in the 8 nm sample relative to the 28 nm sample, where the 8 nm sample discharge region appears to be comprised of more areas of smaller size. More detailed quantitative analysis was done to determine the size distributions of the discharged regions using ImageJ software.[37] The entire TXM image (Figures 9 and 10) was analyzed in each case, however, selected areas are magnified for clarity (Figures 9A–C and 10A–C) and to illustrate the image processing process. A threshold was applied in order to distinguish red (discharged) regions of the Fe_3O_4 agglomerates from the undischarged (green) regions and the regions without Fe_3O_4. In total, 1238 discharged regions (defined as one or more adjacent red pixels) were analyzed for the 28 nm Fe_3O_4 electrode, while 2856 regions were analyzed for the 8 nm sample. For the 28 nm sample, the mean and median size of the discharged regions were 0.26 and 0.17 μm, respectively, while for the 8 nm sample, the mean and median size of the discharged regions were 0.19 and 0.15 μm, respectively. To further illustrate the differences, the data for the discharge regions were sorted by size and compartmentalized in bins of 0–0.01, 0.01–0.1, and 0.1–1 μm. The histograms indicate that discharged regions greater than 0.1 μm comprise >40% of the total discharge region for the 28 nm sample, but <13% for the 8 nm sample (Figure 11). Thus, the TXM-XANES images suggest a more evenly distributed and uniform discharge for the smaller crystallite size Fe_3O_4.

DOI: 10.1021/acsami.5b02478
ACS Appl. Mater. Interfaces 2015, 7, 13457–13466

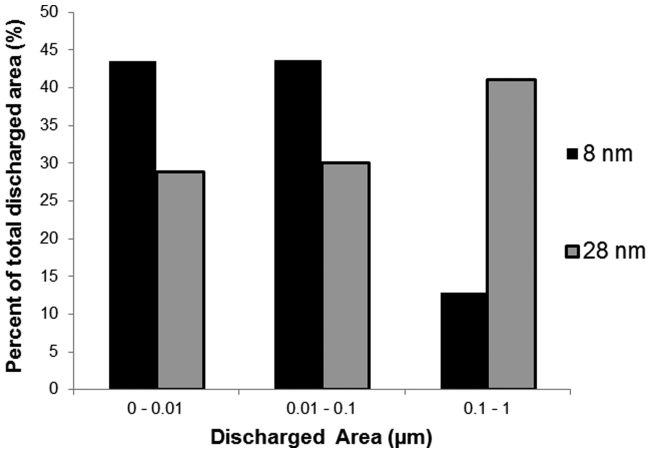

Figure 11. Size distribution of discharged regions from TXM-XANES images.

SUMMARY

The results from this study reveal several significant findings. We were successful in direct observation of crystallites and agglomerates of magnetite (Fe_3O_4) in functional battery electrodes, including 2D cross sectional analysis by transmission electron microscopy (TEM) and transmission X-ray microscopy (TXM). Further, this study yielded the unexpected outcome that the agglomerate sizes of the magnetite within the composite electrodes did not relate to crystallite size of the parent Fe_3O_4 material. Since the magnetite agglomerate size is approximately constant for the two composite electrodes and the agglomerate distributions are also similar, the observed differences in electrochemistry can be attributed directly to crystallite size. In our study, the smaller crystallites are observed to discharge in a more even fashion relative to the larger crystallites, which provides a clear rationale consistent with the enhanced rate capability of the smaller crystallite composite electrodes. The above observations provide a clear rationale for future composite electrode studies using our reported characterization strategy, since differences in agglomerate sizes and agglomerate distributions need to be observed and then electrochemically probed in other families of composite electrodes, particularly for electrochemically active nanomaterials.

ASSOCIATED CONTENT

Supporting Information

Normalized absorption spectra of Fe_3O_4 and FeO reference materials. The Supporting Information is available free of charge on the ACS Publications website at DOI: 10.1021/acsami.5b02478.

AUTHOR INFORMATION

Corresponding Authors

*E-mail: amy.marschilok@stonybrook.edu.
*E-mail: kenneth.takeuchi.1@stonybrook.edu.
*E-mail: esther.takeuchi@stonybrook.edu.

Author Contributions

The manuscript was written through contributions of all authors. All authors have given approval to the final version of the manuscript.

Notes

The authors declare no competing financial interest.

ACKNOWLEDGMENTS

This work was supported as part of the Center for Mesoscale Transport Properties, an Energy Frontier Research Center supported by the U.S. Department of Energy, Office of Science, Basic Energy Sciences, under award DE-SC0012673. The use of the NSLS and TEM facility at the Center for Functional Nanomaterials was supported by the U.S. Department of Energy, Office of Basic Energy Science under contract number DE-AC02-98CH10886. K. Kirshenbaum acknowledges Postdoctoral support from Brookhaven National Laboratory and the Gertrude and Maurice Goldhaber Distinguished Fellowship Program. The authors acknowledge the Transmission Electron Microscopy Facility in the Central Microscopy Imaging Center (C-MIC) at Stony Brook University, Stony Brook, New York for their contribution towards the TEM preparation and data collection.

REFERENCES

(1) Bock, D. C.; Marschilok, A. C.; Takeuchi, K. J.; Takeuchi, E. S. Batteries Used to Power Implantable Biomedical Devices. *Electrochim. Acta* **2012**, *84*, 155−164.

(2) Soloveichik, G. L., Battery Technologies for Large-Scale Stationary Energy Storage. In *Annual Review of Chemical and Biomolecular Engineering*, Vol. 2; Prausnitz, J. M., Ed.; Annual Reviews: Palo Alto, CA, 2011; pp 503−527.

(3) Jin, Y. C.; Lu, M. I.; Wang, T. H.; Yang, C. R.; Duh, J. G. Synthesis of High-Voltage Spinel Cathode Material with Tunable Particle Size and Improved Temperature Durability for Lithium Ion Battery. *J. Power Sources* **2014**, *262*, 483−487.

(4) Rai, A. K.; Anh, L. T.; Gim, J.; Mathew, V.; Kang, J.; Paul, B. J.; Song, J.; Kim, J. Simple Synthesis and Particle Size Effects of TiO_2 Nanoparticle Anodes for Rechargeable Lithium Ion Batteries. *Electrochim. Acta* **2013**, *90*, 112−118.

(5) Cui, J. F.; Qing, C. X.; Zhang, Q. T.; Su, C.; Wang, X. M.; Yang, B. P.; Huang, X. B. Effect of the Particle Size on the Electrochemical Performance of Nano-Li_2FeSiO_4/C Composites. *Ionics* **2014**, *20*, 23−28.

(6) Wagemaker, M.; Mulder, F. M. Properties and Promises of Nanosized Insertion Materials for Li-Ion Batteries. *Acc. Chem. Res.* **2013**, *46*, 1206−1215.

(7) Duan, H.; Gnanaraj, J.; Liang, J. Synthesis and Rate Performance of Fe_3O_4-Based Cu Nanostructured Electrodes for Li Ion Batteries. *J. Power Sources* **2011**, *196*, 4779−4784.

(8) Larcher, D.; Masquelier, C.; Bonnin, D.; Chabre, Y.; Masson, V.; Leriche, J. B.; Tarascon, J. M. Effect of Particle Size on Lithium Intercalation into Alpha-Fe_2O_3. *J. Electrochem. Soc.* **2003**, *150*, A133−A139.

(9) Poizot, P.; Laruelle, S.; Grugeon, S.; Dupont, L.; Tarascon, J. M. Nano-Sized Transition-Metal Oxides as Negative-Electrode Materials for Lithium-Ion Batteries. *Nature* **2000**, *407*, 496−499.

(10) Xiong, Q. Q.; Tu, J. P.; Lu, Y.; Chen, J.; Yu, Y. X.; Qiao, Y. Q.; Wang, X. L.; Gu, C. D. Synthesis of Hierarchical Hollow-Structured Single-Crystalline Magnetite (Fe_3O_4) Microspheres: The Highly Powerful Storage Versus Lithium as an Anode for Lithium Ion Batteries. *J. Phys. Chem. C* **2012**, *116*, 6495−6502.

(11) Okubo, M.; Hosono, E.; Kim, J.; Enomoto, M.; Kojima, N.; Kudo, T.; Zhou, H.; Honma, I. Nanosize Effect on High-Rate Li-Ion Intercalation in $LiCoO_2$ Electrode. *J. Am. Chem. Soc.* **2007**, *129*, 7444−7452.

(12) Xue, L.; Li, X.; Liao, Y.; Xing, L.; Xu, M.; Li, W. Effect of Particle Size on Rate Capability and Cyclic Stability of $LiNi_{0.5}Mn_{1.5}O_4$ Cathode for High-Voltage Lithium Ion Battery. *J. Solid State Electrochem.* **2014**, *19*, 569−576.

(13) Zheng, J.-c.; Li, X.-h.; Wang, Z.-x.; Guo, H.-j.; Zhou, S.-y. $LiFePO_4$ with Enhanced Performance Synthesized by a Novel Synthetic Route. *J. Power Sources* **2008**, *184*, 574−577.

DOI: 10.1021/acsami.5b02478
ACS Appl. Mater. Interfaces 2015, 7, 13457−13466

(14) Zhu, S.; Marschilok, A. C.; Lee, C.-Y.; Takeuchi, E. S.; Takeuchi, K. J. Synthesis and Electrochemistry of Silver Hollandite. *Electrochem. Solid-State Lett.* **2010**, *13*, A98−A100.
(15) Takeuchi, K. J.; Yau, S. Z.; Menard, M. C.; Marschilok, A. C.; Takeuchi, E. S. Synthetic Control of Composition and Crystallite Size of Silver Hollandite, $Ag_xMn_8O_{16}$: Impact on Electrochemistry. *ACS Appl. Mater. Interfaces* **2012**, *4*, 5547−5554.
(16) Takeuchi, K. J.; Yau, S. Z.; Subramanian, A.; Marschilok, A. C.; Takeuchi, E. S. The Electrochemistry of Silver Hollandite Nanorods, $Ag_xMn_8O_{16}$: Enhancement of Electrochemical Battery Performance Via Dimensional and Compositional Control. *J. Electrochem. Soc.* **2013**, *160*, A3090−A3094.
(17) Komaba, S.; Mikumo, T.; Ogata, A. Electrochemical Activity of Nanocrystalline Fe_3O_4 in Aprotic Li and Na Salt Electrolytes. *Electrochem. Commun.* **2008**, *10*, 1276−1279.
(18) Komaba, S.; Mikumo, T.; Yabuuchi, N.; Ogata, A.; Yoshida, H.; Yamada, Y. Electrochemical Insertion of Li and Na Ions into Nanocrystalline Fe_3O_4 and Alpha-Fe_2O_3 for Rechargable Batteries. *J. Electrochem. Soc.* **2010**, *157*, A60−A65.
(19) Zhu, S.; Marschilok, A. C.; Takeuchi, E. S.; Takeuchi, K. J. Crystallite Size Control and Resulting Electrochemistry of Magnetite, Fe_3O_4. *Electrochem. Solid-State Lett.* **2009**, *12*, A91−A94.
(20) Zhu, S.; Marschilok, A. C.; Takeuchi, E. S.; Yee, G. T.; Wang, G.; Takeuchi, K. J. Nanocrystalline Magnetite: Synthetic Crystallite Size Control and Resulting Magnetic and Electrochemical Properties. *J. Electrochem. Soc.* **2010**, *157*, A1158−A1163.
(21) Sasaki, S. Radial Distribution of Electron Density in Magnetite, Fe_3O_4. *Acta Crystallogr., Sect. B Struct. Sci.* **1997**, *B53*, 762−766.
(22) Menard, M. C.; Marschilok, A. C.; Takeuchi, K. J.; Takeuchi, E. S. Variation in the Iron Oxidation States of Magnetite Nanocrystals as a Function of Crystallite Size: The Impact on Electrochemical Capacity. *Electrochim. Acta* **2013**, *94*, 320−326.
(23) Menard, M. C.; Takeuchi, K. J.; Marschilok, A. C.; Takeuchi, E. S. Electrochemical Discharge of Nanocrystalline Magnetite: Structure Analysis Using X-Ray Diffraction and X-Ray Absorption Spectroscopy. *Phys. Chem. Chem. Phys.* **2013**, *15*, 18539−18548.
(24) Marschilok, A. C.; Schaffer, C. P.; Takeuchi, K. J.; Takeuchi, E. S. Carbon Nanotube-Metal Oxide Composite Electrodes for Secondary Lithium-Based Batteries. *J. Compos Mater.* **2013**, *47*, 41−49.
(25) Cornut, R.; Lepage, D.; Schougaard, S. B. Ohmic Drop in $LiFePO_4$ Based Lithium Battery Cathodes Containing Agglomerates. *J. Electrochem. Soc.* **2012**, *159*, A822−A827.
(26) Li, J. L.; Armstrong, B. L.; Kiggans, J.; Daniel, C.; Wood, D. L. Lithium Ion Cell Performance Enhancement Using Aqueous $LiFePO_4$ Cathode Dispersions and Polyethyleneimine Dispersant. *J. Electrochem. Soc.* **2013**, *160*, A201−A206.
(27) Bhattacharya, S.; Riahi, A. R.; Alpas, A. T.; Transmission, A. Electron Microscopy Study of Crack Formation and Propagation in Electrochemically Cycled Graphite Electrode in Lithium-Ion Cells. *J. Power Sources* **2011**, *196*, 8719−8727.
(28) Brazier, A.; Dupont, L.; Dantras-Laffont, L.; Kuwata, N.; Kawamura, J.; Tarascon, J. M. First Cross-Section Observation of an All Solid-State Lithium-Ion "Nanobattery" by Transmission Electron Microscopy. *Chem. Mater.* **2008**, *20*, 2352−2359.
(29) Klingele, M.; Zengerle, R.; Thiele, S. Quantification of Artifacts in Scanning Electron Microscopy Tomography: Improving the Reliability of Calculated Transport Parameters in Energy Applications Such as Fuel Cell and Battery Electrodes. *J. Power Sources* **2015**, *275*, 852−859.
(30) Li, C. Y. V.; Wang, Z. M.; Liu, S.; Chan, S. L. I. Electrochemical Characteristics of La-Ni-Al Thin Films. *J. Alloys Compd.* **2008**, *456*, 407−412.
(31) Neversa, D. R.; Peterson, S. W.; Robertson, L.; Chubbuck, C.; Flygare, J.; Cole, K.; Wheeler, D. R. The Effect of Carbon Additives on the Microstructure and Conductivity of Alkaline Battery Cathodes. *J. Electrochem. Soc.* **2014**, *161*, A1691−A1697.
(32) Stephenson, D. E.; Walker, B. C.; Skelton, C. B.; Gorzkowski, E. P.; Rowenhorst, D. J.; Wheeler, D. R. Modeling 3D Microstructure and Ion Transport in Porous Li-Ion Battery Electrodes. *J. Electrochem. Soc.* **2011**, *158*, A781−A789.
(33) Wilson, J. R.; Cronin, J. S.; Barnett, S. A.; Harris, S. J. Measurement of Three-Dimensional Microstructure in a $LiCoO_2$ Positive Electrode. *J. Power Sources* **2011**, *196*, 3443−3447.
(34) Zhang, H. L.; Li, F.; Liu, C.; Tan, J.; Cheng, H. M. New Insight into the Solid Electrolyte Interphase with Use of a Focused Ion Beam. *J. Phys. Chem. B* **2005**, *109*, 22205−22211.
(35) Zier, M.; Scheiba, F.; Oswald, S.; Thomas, J.; Goers, D.; Scherer, T.; Klose, M.; Ehrenberg, H.; Eckert, J. Lithium Dendrite and Solid Electrolyte Interphase Investigation Using OsO_4. *J. Power Sources* **2014**, *266*, 198−207.
(36) Muto, S.; Sasano, Y.; Tatsumi, K.; Sasaki, T.; Horibuchi, K.; Takeuchi, Y.; Ukyo, Y. Capacity-Fading Mechanisms of $LiNiO_2$-Based Lithium-Ion Batteries. *J. Electrochem. Soc.* **2009**, *156*, A371−A377.
(37) Schneider, C. A.; Rasband, W. S.; Eliceiri, K. W. NIH Image to ImageJ: 25 Years of Image Analysis. *Nat. Methods* **2012**, *9*, 671−675.
(38) Scherrer, P. Estimation of the Size and Internal Structure of Colloidal Particles by Means of Rontgen Rays. *Nachr. Ges. Wiss. Gottingen* **1918**, 96−100.
(39) Patterson, A. L. The Scherrer Formula for X-Ray Particle-Size Determination. *Phys. Rev.* **1939**, *56*, 978−82.
(40) Al-Ostaz, A.; Diwakar, A.; Alzebdeh, K. I. Statistical Model for Characterizing Random Microstructure of Inclusion-Matrix Composites. *J. Mater. Sci.* **2007**, *42*, 7016−7030.
(41) Borbely, A.; Csikor, F. F.; Zabler, S.; Cloetens, P.; Biermann, H. Three-Dimensional Characterization of the Microstructure of a Metal-Matrix Composite by Holotomography. *Mater. Sci. Eng., A* **2004**, *367*, 40−50.
(42) Ghosh, S.; Nowak, Z.; Lee, K. Quantitative Characterization and Modeling of Composite Microstructures by Voronoi Cells. *Acta Mater.* **1997**, *45*, 2215−2234.
(43) Karnezis, P. A.; Durrant, G.; Cantor, B. Characterization of Reinforcement Distribution in Cast Al-Alloy/Sicp Composites. *Mater. Charact.* **1998**, *40*, 97−109.
(44) Saheb, N.; Ul Qadir, N.; Siddiqui, M. U.; Arif, A. F. M.; Akhtar, S. S.; Al-Aqeeli, N. Characterization of Nanoreinforcement Dispersion in Inorganic Nanocomposites: A Review. *Materials* **2014**, *7*, 4148−4181.
(45) Yang, N.; Boselli, J.; Sinclair, I. Simulation and Quantitative Assessment of Homogeneous and Inhomogeneous Particle Distributions in Particulate Metal Matrix Composites. *J. Microsc. (Oxford, U. K.)* **2001**, *201*, 189−200.
(46) Clark, P. J.; Evans, F. C. Distance to Nearest Neighbor as a Measure of Spatial Relationships in Populations. *Ecology* **1954**, *35*, 445−453.
(47) Hui, L.; Smith, R. C.; Wang, X.; Nelson, J. K.; Schadler, L. S. Quantification of Particulate Mixing in Nanocomposites. *IEEE Conf. Electr. Insul. Dielectr. Phenom.* **2008**, 272−275.
(48) Faiyas, A. P. A.; Vinod, E. M.; Joseph, J.; Ganesan, R.; Pandey, R. K. Dependence of pH and Surfactant Effect in the Synthesis of Magnetite (Fe_3O_4) Nanoparticles and Its Properties. *J. Magn. Magn. Mater.* **2010**, *322*, 400−404.
(49) Goya, G. F.; Berquo, T. S.; Fonseca, F. C.; Morales, M. P. Static and Dynamic Magnetic Properties of Spherical Magnetite Nanoparticles. *J. Appl. Phys.* **2003**, *94*, 3520−3528.
(50) Fleet, M. E. The Structure of Magnetite: Symmetry of Cubic Spinels. *J. Solid State Chem.* **1986**, *62*, 75−82.
(51) Fontcuberta, J.; Rodriguez, J.; Pernet, M.; Longworth, G.; Goodenough, J. B. Structural and Magnetic Characterization of the Lithiated Iron Oxide $Li_xFe_3O_4$. *J. Appl. Phys.* **1986**, *59*, 1918−1926.
(52) Thackeray, M. M.; David, W. I. F.; Goodenough, J. B. Structural Characterization of the Lithiated Iron Oxides $Li_xFe_3O_4$ and $Li_xFe_2O_3$ ($0 < x < 2$). *Mater. Res. Bull.* **1982**, *17*, 785−793.
(53) Bard, A. J.; Faulkner, L. R. *Electrochemical Methods: Fundamentals and Applications*; Wiley: New York, 2000.
(54) Boesenberg, U.; Meirer, F.; Liu, Y. J.; Shukla, A. K.; Dell'Anna, R.; Tyliszczak, T.; Chen, G. Y.; Andrews, J. C.; Richardson, T. J.; Kostecki, R.; Cabana, J. Mesoscale Phase Distribution in Single

DOI: 10.1021/acsami.5b02478
ACS Appl. Mater. Interfaces 2015, 7, 13457−13466

Particles of $LiFePO_4$ Following Lithium Deintercalation. *Chem. Mater.* **2013**, *25*, 1664−1672.
(55) Chao, S. C.; Song, Y. F.; Wang, C. C.; Sheu, H. S.; Wu, H. C.; Wu, N. L. Study on Microstructural Deformation of Working Sn and SnSb Anode Particles for Li-Ion Batteries by in Situ Transmission X-Ray Microscopy. *J. Phys. Chem. C* **2011**, *115*, 22040−22047.
(56) Gonzalez-Jimenez, I. D.; Cats, K.; Davidian, T.; Ruitenbeek, M.; Meirer, F.; Liu, Y. J.; Nelson, J.; Andrews, J. C.; Pianetta, P.; de Groot, F. M. F.; Weckhuysen, B. M. Hard X-Ray Nanotomography of Catalytic Solids at Work. *Angnew. Chem., Int. Ed.* **2012**, *51*, 11986−11990.
(57) Sakdinawat, A.; Attwood, D. Nanoscale X-Ray Imaging. *Nat. Photonics* **2010**, *4*, 840−848.
(58) Wang, J.; Chen, Y. C. K.; Yuan, Q. X.; Tkachuk, A.; Erdonmez, C.; Hornberger, B.; Feser, M. Automated Markerless Full Field Hard X-Ray Microscopic Tomography at Sub-50-nm 3-Dimension Spatial Resolution. *Appl. Phys. Lett.* **2012**, *100*, No. 143107.
(59) Wang, J. J.; Chen-Wiegart, Y. C. K.; Wang, J. In Situ Chemical Mapping of a Lithium-Ion Battery Using Full-Field Hard X-Ray Spectroscopic Imaging. *Chem. Commun.* **2013**, *49*, 6480−6482.
(60) Wang, J. J.; Chen-Wiegart, Y. C. K.; Wang, J. In Situ Three-Dimensional Synchrotron X-Ray Nanotomography of the (De)-Lithiation Processes in Tin Anodes. *Angew. Chem., Int. Ed.* **2014**, *53*, 4460−4464.
(61) Wang, J. J.; Chen-Wiegart, Y. C. K.; Wang, J. *In Operando* Tracking Phase Transformation Evolution of Lithium Iron Phosphate with Hard X-Ray Microscopy. *Nat. Commun.* **2014**, *5*, No. 4570.
(62) Yang, F. F.; Liu, Y. J.; Martha, S. K.; Wu, Z. Y.; Andrews, J. C.; Ice, G. E.; Pianetta, P.; Nanda, J. Nanoscale Morphological and Chemical Changes of High Voltage Lithium Manganese Rich NMC Composite Cathodes with Cycling. *Nano Lett.* **2014**, *14*, 4334−4341.

DOI: 10.1021/acsami.5b02478
ACS Appl. Mater. Interfaces 2015, 7, 13457−13466